Toward nonlinear magnonics: Intensity-dependent spin-wave switching in insulating side-coupled magnetic stripes

A. V. Sadovnikov*
Laboratory "Metamaterials", Saratov State University, Saratov 410012, Russia
and Kotel'nikov Institute of Radioengineering and Electronics, Russian Academy of Sciences, Moscow 125009, Russia

S. A. Odintsov, E. N. Beginin, S. E. Sheshukova, and Yu. P. Sharaevskii
Laboratory "Metamaterials", Saratov State University, Saratov 410012, Russia

S. A. Nikitov
Laboratory "Metamaterials", Saratov State University, Saratov 410012, Russia
and Kotel'nikov Institute of Radioengineering and Electronics, Russian Academy of Sciences, Moscow 125009, Russia
(Received 5 May 2017; revised manuscript received 8 September 2017; published 24 October 2017)

We demonstrate that the nonlinear spin-wave transport in two laterally parallel magnetic stripes exhibit the intensity-dependent power exchange between the adjacent spin-wave channels. By the means of Brillouin light scattering technique, we investigate collective nonlinear spin-wave dynamics in the presence of magnetodipolar coupling. The nonlinear intensity-dependent effect reveals itself in the spin-wave mode transformation and differential nonlinear spin-wave phase shift in each adjacent magnetic stripe. The proposed analytical theory, based on the coupled Ginzburg-Landau equations, predicts the geometry design involving the reduction of power requirement to the all-magnonic switching. A very good agreement between calculation and experiment was found. In addition, a micromagnetic and finite-element approach has been independently used to study the nonlinear behavior of spin waves in adjacent stripes and the nonlinear transformation of spatial profiles of spin-wave modes. Our results show that the proposed spin-wave coupling mechanism provides the basis for nonlinear magnonic circuits and opens the perspectives for all-magnonic computing architecture.

DOI: 10.1103/PhysRevB.96.144428

I. INTRODUCTION

In the past decades, the patterning of insulating magnetic materials emerges as a promising technology which is the basis of the rising field of magnonics and magnon-spintronics for magnonic integrated circuits (see, e.g., Refs. [1–5] and references therein).

The insulating-based magnonics opens a promising alternative to the concept of beyond-CMOS signal processing devices [4,6–8], in which information is carried by spin waves (SW) (or magnons) instead of electrons. The ferrimagnetic thin films of yttrium iron garnet (YIG) possess significantly smaller dynamic spin-wave damping compared to the metallic magnetic films (even for the case of the nanometer-thick YIG [9]). Thus utilization of the patterned YIG provides the basis for next generation computing technology with low-level energy consumption [1,4].

The particular problem of each signal processing device inside the magnonic network is the fabrication of the spin-wave buses, which connect the functional magnonic units together. The interconnection can be realized with the magnonic waveguides [10], irregular magnetic structures [11], and via the dipolar coupling of spin waves. The latter is performed via two types of the magnonic architectures: the vertical [12–14] and planar or lateral [15–18] topologies of the magnonic network. The vertical coupling of spin waves is usually implemented in the sandwiched multilayer magnetic structure [14], whereas the lateral topology implies the using of side-coupled magnonic stripe (SCMS).

The latter is the routine versatile component with great potential for integration into large-scale planar magnonic circuits and suitable for versatile operations with data in magnonic networks due to the controllable collective magnetization dynamics in the adjacent ferromagnetic stripes [16,19–23]. SCMSs provide the magnonic interconnects of separate magnonic signal processing elements in the magnonic networks [2,17] and can operate as the multichannel directional coupler [16,19–21], spin-wave power splitter [22], and tunable frequency-selective insulating-based magnonic unit [11,18].

The interest in nonlinear spin-wave processes in ferromagnets has arisen from the evolution of the theory of nonlinear dynamics of dissipative systems [24–26]. Such nonlinear phenomena in YIG as two-dimensional wave bullets and soliton formation and propagation have been traditionally studied in spin-wave waveguides of millimeter width using microwave [27–31] and Brillouin light scattering techniques [32–41]. By employing the nonlinear effects in YIG [27–29,42], the variety of tunable spin-wave devices was realized [32,33,37,38,40,43], e.g., intensity-dependent nonlinear phase shifters, filters [44–46], and magnonic-crystal based switching devices [22]. In recent years the nonlinear spin-wave dynamics has drawn great attention as a new means for generation of coherent spin-wave modes by spin-orbit torque produced by pure spin currents [9,43].

An alternative mechanism of spin-wave switching can be implemented by the means of the SCMSs integration in the insulator-based circuits providing the control of the

*sadovnikovav@gmail.com

magnetization switching by the spin-wave intensity. However, it should be noted that the lateral confinement of magnetic stripes results both in the complicated nonlinear dynamics of SW and multimode spin-wave coupling in lateral topology. Therefore, investigation of the interplay between the spin-wave coupling and nonlinearities in confined magnetic structures is of significant importance for the physics of all-magnonic ultrafast switching. Moreover, the nonlinear dynamics of coupled spin waves in adjacent magnonic stripes is of importance for nonlinear physics of dissipative systems in general.

Here, we report an experimental investigation of spin-wave intensity-dependent switching in side-coupled magnonic stripes. This behavior is a result of the nonlinear spin-wave mode transformation and differential nonlinear spin-wave phase shift in each adjacent stripe. We present a theoretical model, which describes the nonlinear spin-wave transport in the magnonic stripes in the presence of the magnetodipolar interaction.

The structure of the paper is the following. First, we study the nonlinear spin-wave coupling in the adjacent insulating thin-film ferrimagnet stripe by the means of direct spatially resolved Brillouin light scattering (BLS) technique. We demonstrate that this system provides intensity-dependent switching of spin-wave power between the adjacent stripes (Sec. II). Then, we attribute these effects to the nonlinear behavior of the spin-wave phase and transformation of spin-wave profiles in magnonic stripes. To prove this and describe the weakly nonlinear spatial phenomena in parallel magnetic stripe, we present the simple model based on finite-element method and micromagnetic (Landau-Lifshitz-Gilbert equation) simulation. We show that the experimentally observed variation of the power transmission between magnonic stripes and the power dependency of the coupling length is in agreement with the developed numerical model (Sec. III). Next, we present the phenomenological model based on the space-dependent coupled Ginzburg-Landau equations to describe the main features of the spin-wave coupling in the laterally parallel magnonic stripes taking into account the nonlinear spin-wave damping, and its predictions agree well with the experimental results of both BLS and microwave spectroscopy techniques (Sec. IV). Finally, we discuss the influence of structural parameters on the coupling efficiency and spin-wave switching in Sec. V and show how to decrease the input power, which is enough for an all-magnonic coupler operation. Moreover, we demonstrate that the proposed intensity-dependent dual channel directional coupler can be used for parallel signal processing in nonlinear magnonic networks.

II. EXPERIMENT

A. Structure fabrication

Figure 1(a) shows the schematic of the side-coupled magnonic stripes and the outline of BLS experiment. The adjacent magnetic waveguides were fabricated with the pulsed laser patterning [47] of the $t_1 = 7.7$-μm-thick insulating thin-film ferrimagnet yttrium iron garnet [$Y_3Fe_5O_{12}$ (111)] into the form of side-coupled stripes S_1 and S_2 with edge-to-edge spacing of $d = 40\ \mu$m. YIG film with saturation magnetization of $M_0 = 139$ G was epitaxially grown on a 500-μm-thick gadolinium gallium garnet [$Gd_3Ga_5O_{12}$ (111)] substrate. The width of both stripes was $w = 200\ \mu$m. The length along the long side was 7 mm for S_1 and 5 mm for S_2. The length of the side-coupled region was $b = 5$ mm. These parameters of the SCMSs provide the efficient spin-wave coupling and the optimal switching regime, as it will be explained in Sec. V. The microwave transducer with the width of 30 μm (along x axis) and length of 2 mm (along y axis) was used for spin-waves (SWs) excitation. Input transducer was attached to the stripe S_1. The uniform static magnetic field $H_0 = 1200$ Oe was applied in the plane of the waveguides along the y direction. Thus the guided magnetostatic surface wave (MSSW) was excited [25,48,49].

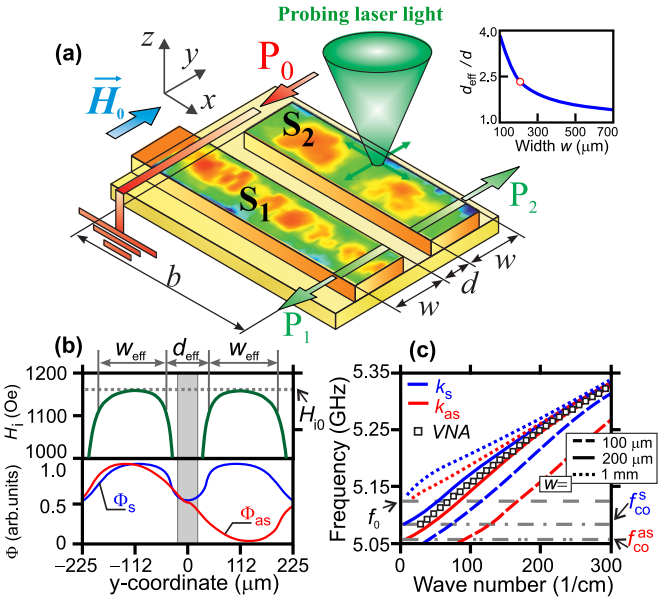

FIG. 1. (a) Schematic view of side-coupled magnonic stripes and cartoon of BLS experiment. BLS measurement was performed in backscattering configuration. On the inset: relative effective gap d_{eff}/d as a function of stripe's width. (b) Internal magnetic field profile $H_i(y)$ for SCMSs (top) and the transverse profile of the symmetric $\Phi_s(y)$ and antisymmetric $\Phi_{as}(y)$ modes (bottom). The spacing between stripes is depicted with shaded area. (c) The dispersion measured using VNA (open squares) and dispersion characteristics of symmetric and antisymmetric modes of SCMSs of width 100 μm (dashed curves), 200 μm (solid curves), and 1 mm (dotted curves). All the shown data were obtained at $H_0 = 1200$ Oe.

B. Spin-wave dispersion and eigenmode spectra

When two parallel magnetic stripes are brought in close proximity of each other, the propagating SW is coupled by the dipolar field and the spin-wave dispersion branch of an isolated waveguide is split into two SW modes. Thus the eigenmodes spectrum of identical SCMSs consists of the orthogonal system [50] of symmetric Φ_s and antisymmetric Φ_{as} modes [16] [see Fig. 1(c)]. It should be noted that the lateral confinement of adjacent stripes leads not only to the reduction of internal magnetic field H_i but also to the asymmetrical profile of the internal field distribution inside S_1 and S_2 with respect to the center of each stripe [Fig. 1(b), top panel]. As a result, we should take into account the decrease of the

waveguide area, which supports the SW propagation; thus the effective width of each magnonic stripe is $w_{\text{eff}} \approx 150\ \mu$m. Therefore, we use the finite-element method (FEM) [16,51,52] to calculate the eigenmodes spectra and mode profiles of the laterally symmetric parallel magnetic stripes with the nonuniform magnetization configurations inside the stripes. The value of the internal field at the center of both stripes is $H_{i0} = 1159$ Oe. This leads to the redshift of the frequency of ferromagnetic resonance (FMR) of the in-plane magnetized film [53] $f_0 = (\gamma/2\pi)[H_{i0}(H_{i0} + 4\pi M_0)]^{1/2} = 5.141$ GHz, where $\gamma/2\pi = 2.8$ MHz/Oe is the electronic gyromagnetic ratio for YIG.

Figure 1(b), bottom panel, shows the profiles of Φ_s and Φ_{as}. Dispersion characteristics of low order transversal symmetric and antisymmetric modes are shown in Fig. 1(c) with the red and blue lines, respectively. It can be seen that cutoff frequency for the lowest order symmetric mode f_{co}^{s} is higher than that of antisymmetric mode f_{co}^{as} and both frequencies are lower than FMR frequency: $f_{co}^{as} < f_{co}^{s} < f_0$. It is important to emphasize that the increase of the stripe width leads to the reduction of the discrepancy between cutoff and FMR frequencies. Thus, if the width reaches the value $w = 1$ mm, the above-mentioned discrepancy is almost negligible [dotted curves in Fig. 1(c)]; hence $f_{co}^{as} \approx f_{co}^{s} \approx f_0$. Dispersion of MSSW in the SCMS's was measured by microwave technique using E8362C PNA Vector Network Analyzer (VNA). The experiments were performed at relatively small input power $P_0 = -25$ dBm in the linear regime of the MSSW propagation. The output microwave transducer is placed on the S_1 at the distance of 5 mm from the input transducer. Dispersion of MSSW is demonstrated in Fig. 1(c) with open squares. Due to the interference of eigenmodes Φ_s and Φ_{as} the effective wave number of spin wave is equal to $k(f) \approx [k_s(f) + k_{as}(f)]/2$, where k_s and k_{as} are the wave numbers of symmetric and antisymmetric modes.

C. BLS measurements of nonlinear regime of coupled spin-wave propagation

First, to demonstrate the efficient coupling between adjacent magnetic stripes, we use the BLS technique in the backscattering configuration [54–56]. Figure 2 shows the pseudocolor-coded two-dimensional 5×0.45 mm^2 spatial maps of the recorded BLS intensity $I(x,y)$ at the frequency $f_1 = 5.1$ GHz. Intensity map was obtained by the scanning with the probing light spot along the x and y axis with the spatial resolution of 25 μm and then integration over the time period of 2 μs. We perform BLS measurement at different levels of input power $P_0 = -25$ dBm [Fig. 2(a)], $P_0 = 5$ dBm [Fig. 2(b)], and $P_0 = 23$ dBm [Fig. 2(c)]. The input pulse signal had a length of 50 ns. The pulse repetition period was 2 μs.

These parameters of input pulse signal were chosen in order to avoid the overheating of the YIG sample in the area of the input microstrip antenna and self-heating of the YIG sample by the propagating MSSW. Using the VNA and oscilloscope we can estimate the threshold of the pulse width and amplitude at which the frequency starts to shift due to heating. We set the value of power and vary the pulse duration. If the pulse duration at fixed power is sufficiently long to overheat the sample or to induce the four-magnon decay processes, we can determine the appropriate pulse parameters via the recording of the pulse form of reflected signal.

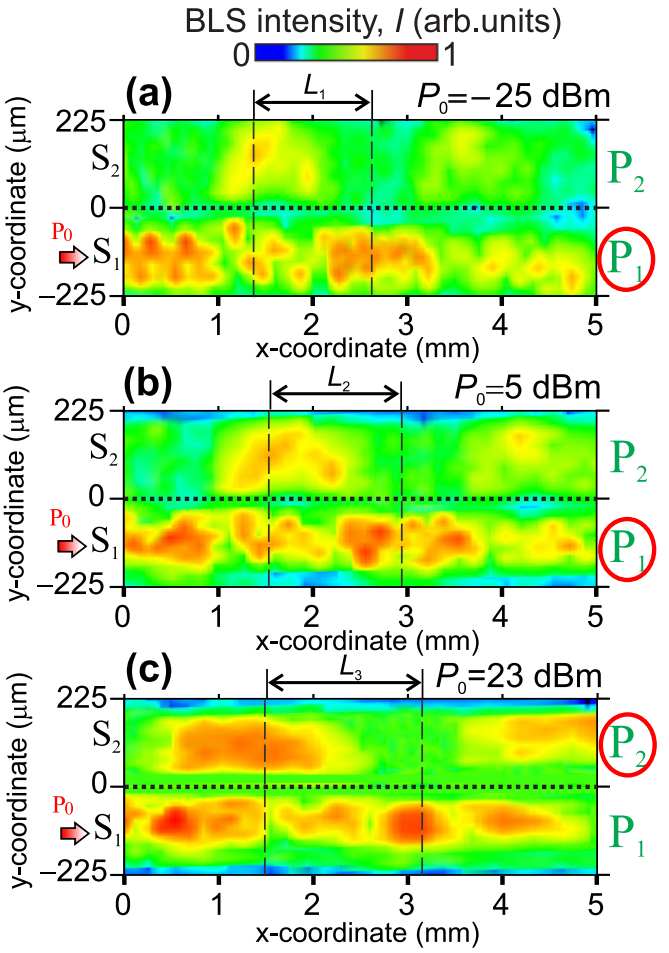

FIG. 2. Normalized color-coded BLS intensity map recorded at the excitation frequency of $f_1 = 5.1$ GHz. Power level of input signal is labeled above each map. Edges of stripes are guided with dotted lines. L denotes the spin-wave coupling length for each map.

From the comparison of these maps, one should note that the spin-wave power transfers from one stripe to the other in a periodic manner with the spatial period of $2L$. Here L is the coupling length, which is equal to the distance along x direction over which a SW propagating in one magnonic stripe transfers all its energy to the second adjacent stripe. Coupling length is defined at the frequency f and power P_0 as $L(f,P_0) = \pi/|k_s(f,P_0) - k_{as}(f,P_0)|$, where $k_s(f,P_0)$ and $k_{as}(f,P_0)$ are the wave numbers of the lowest order transversal symmetric and antisymmetric modes.

It is also worth noting that the results presented in Fig. 2 show that L is increased with the increase of the input power level. Thus the BLS experiment reveals the nonlinear nature of the intensity-dependent switching. Therefore, the SW may be effectively routed between the magnetic stripes by changing input power. Hereafter we propose the explanation of this nonlinear effect. We denote the coupling length, extracted from BLS data as $L_{1,2,3}$ (see Fig. 2), where L_1 corresponds to the linear regime ($P_0 = -25$ dBm), L_2 to $P_0 = 5$ dBm, and L_3 to $P_0 = 23$ dBm.

One should take into account that the full power exchange between S_1 and S_2 is unachievable due to the different coupling lengths of the transverse width modes [16]. Figures 2(a) and 2(b) demonstrate also that for a given excitation frequency f_1 only the first and second width modes in S_2 interfere with each other [57]. This leads to the formation of "snake-like" stationary intensity distribution in S_2. Therefore, SCMS can operate as a width-mode sorter, which is similar to the symmetry-broken magnonic waveguide [58]. As the input power level is increased the spin-wave intensity distribution in each stripe transforms due to the nonlinear coupling between initially independent width modes [39]. Thus the proposed topology of the SCMSs can act as an all-magnonic equivalent of a tunable multiferroic coupler [23], similar to all-optical switching in the fiber couplers [59–63] or in the graphene layers [64].

III. MECHANISM OF SPIN-WAVE COUPLING IN ADJACENT STRIPES

A. Linear regime of spin-wave coupling

Next, to elucidate the intermodal coupling mechanism between the stripes, we perform the micromagnetic study (MMS) of spin-wave propagation along the side-coupled waveguides (see Fig. 3). We use the object-oriented micromagnetic framework (OOMMF) [65] to perform the numerical solution of a Landau-Lifshitz equation for the dynamics of the magnetization [66]. The volume of simulation area was $(7000 \times 440 \times 7.7)\ \mu\text{m}^3$; the size of the mesh cell was $(0.1 \times 0.1 \times 1.1)\ \mu\text{m}^3$. First, we perform the static simulation to obtain the ground magnetic state of coupled stripes. Therefore, we define the internal magnetic field profile $H_i(y)$ [see Fig. 1(b), top panel]. The reason for using MMS to describe the magnetodipolar coupling of spin waves is in the straightforward possibility to compute the intensity-dependent magnetization dynamics in the case of nonuniform $H_i(y)$. In the next step of the micromagnetic simulations, spin waves were excited in the vicinity of the left edge of S_1 by a local magnetic field of harmonic temporal profile $h(x,z,t) = h_0 \sin(2\pi f t)[h_x(x,z)\vec{x}_0 + h_z(x,z)\vec{z}_0]$, where h_0 is the amplitude of dynamic magnetization; the x and z profiles of dynamic magnetic field were taken into account [67,68] with $h_x(x,z)$ and $h_z(x,z)$, respectively.

Figure 3(a) demonstrates the dynamic out-of-plane component of magnetization m_z inside the $5 \times 0.45\ \text{mm}^2$ box. Snapshot was extracted after a lapse of 100 ns from the onset of the excitation at the frequency of 5.1 GHz and amplitude $h_0 = 10^{-5}$ Oe. The chosen parameters correspond to the $P_0 = -25$ dBm in experimental setup and, therefore, to the linear regime of SW propagation.

By the means of the Hilbert transform [69] we detect the envelope of the dynamic magnetization $\Psi(x,y)$ [see Fig. 3(b)]. Hence we are able to plot the envelope of the dynamic magnetization across the x coordinate inside each film as $\Psi_1(x) = \int_0^w \Psi(y,x)\,dy$ and $\Psi_2(x) = \int_{w+d}^{2w+d} \Psi(y,x)\,dy$. Figure 3(c) summarizes the results obtained from BLS microscopy measurements (open symbols) and micromagnetic simulations (solid curves) of longitudinal spin-wave profiles in each adjacent stripe. The results of BLS measurement of $I_1(x) = \int_0^w I(y,x)\,dy$ and $I_2(x) = \int_{w+d}^{2w+d} I(y,x)\,dy$ are shown in Fig. 3(c) with open squares and circles, respectively, and are strikingly similar to the results of simulation. Thus the coupling length can be estimated from the well-pronounced dips in the $\Psi_1(x)$ and $\Psi_2(x)$ as well as in $I_1(x)$ and $I_2(x)$. The value of L is monotonically increased with the increase of the SW frequency [open squares in Fig. 3(d)]. This is well confirmed by the numerical simulation [dashed curve in Fig. 3(d)].

B. Nonlinear regime of spin-wave coupling

Next, to reveal the nonlinear regime of spin-wave coupling we plot the coupling length as a function of input power from

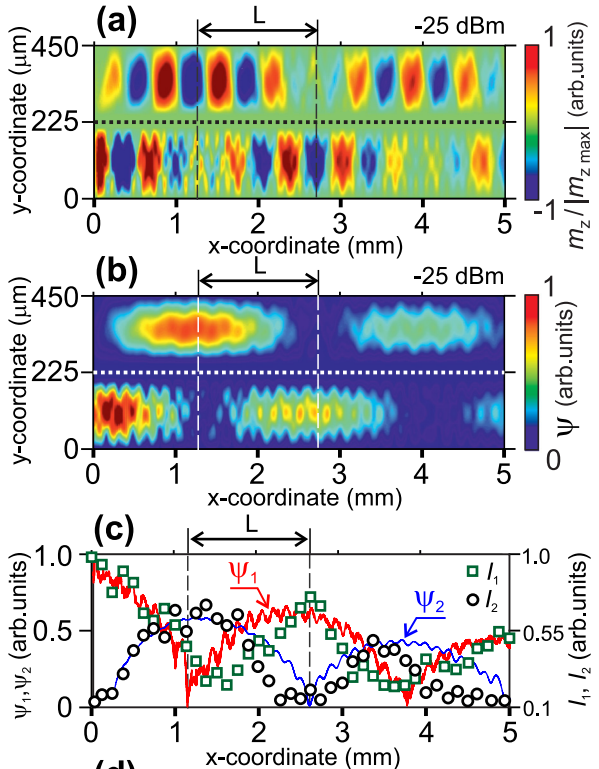

FIG. 3. Snapshots of the out-of-plane component of dynamic magnetization (a) and distribution of spin-wave amplitude (b) calculated by the means of micromagnetic simulations at the excitation frequency of $f_1 = 5.1$ GHz. Edges of stripes are guided with dotted lines. (c) Calculated longitudinal profile of spin-wave amplitude in first (Ψ_1) and second (Ψ_2) stripe. The data of BLS experiment are shown with open symbols. (d) Frequency dependence of L is shown with open circles (BLS data), solid curve (micromagnetic simulation), and dotted curve (FEM simulation). All the shown data were obtained at $H_0 = 1200$ Oe.

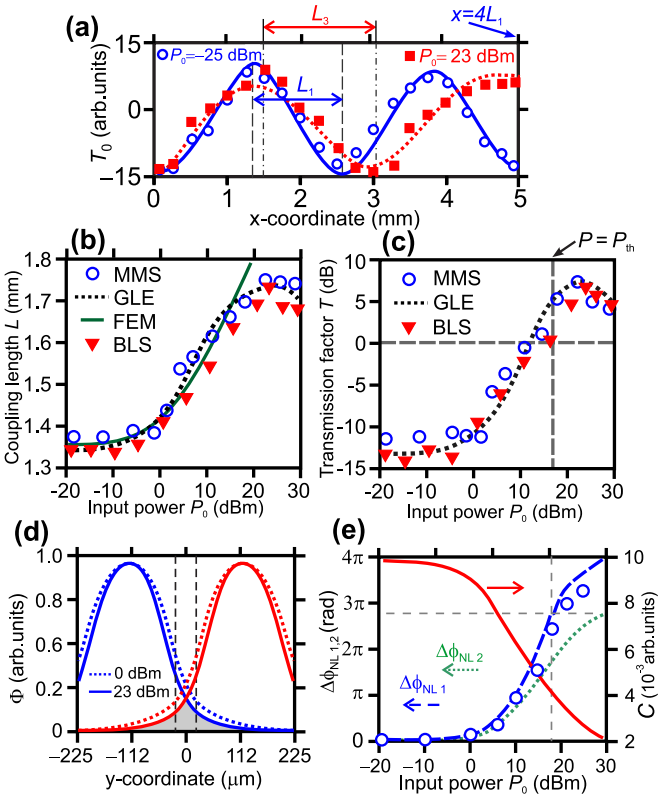

FIG. 4. (a) Experimentally measured transmission coefficient T_0 as a function of x coordinate at $P_0 = -25$ dBm (open circles) and $P_0 = 23$ dBm (closed squares). Solid and dashed curves depict the results of numerical simulation; power dependency of coupling length (b) and transmission factor (c), measured by BLS (triangles) and numerically simulated using micromagnetic simulation (MMS), FEM, and coupled GLEs (as labeled in box). (d) Mode y profiles $\Phi_{1,2}$ of separated stripes at $P_0 = 0$ dBm (dashed curve) and $P_0 = 23$ dBm (solid curves). (e) Nonlinear differential phase shift in each stripe $\Delta\phi_{NL1,2}$ (dashed and dotted curves) and overlap integral C (solid curve) as a function of input power. The data were obtained for $f = 5.1$ GHz and $H_0 = 1200$ Oe.

the experimentally measured BLS map [see the red triangles in Fig. 4(b)]. These data clearly demonstrate the increase of coupling length by the factor of 1.3, which is enough for the spin-wave power switching between the adjacent stripes in the magnonic circuits. The ratio of power transferred from S_1 to S_2 at each value of x coordinate can be estimated via coefficient $T_0 = 10\log(P_2/P_1)$, where $P_{1,2} = I_{1,2}(x)$ are the integrated BLS intensities across each stripe. The variation of the T_0 across the x coordinate is plotted with open circles in linear regime and closed squares in nonlinear regime [see Fig. 4(a)]. It is seen that the position-dependent coefficient T_0 is not convenient for the generality of the nonlinear coupling description. Thus the efficiency of power transfer between magnonic stripes can be estimated with the coefficient T, which is defined as $T = 10\log(P_2/P_1)$, where $P_{1,2} = I_{1,2}(x = 4L_1)$ are the integrated BLS intensities across $S_{1,2}$ at $x = 4L_1$. We emphasize that this way of definition of T is convenient for the nonlinear coupler operation description. Thus the position independent coefficient T is defined mainly by the spin-wave dispersion. Therefore, T describes mainly the transformation of spin-wave characteristics in the nonlinear regime against the linear regime. With the input power increasing, the spin-wave power is switched from S_1 into S_2 (Fig. 2) and T increases by 15 dB in going from $P_0 = -20$ dBm to $P_0 = 20$ dBm. We note that the spin-wave power is divided equally between the magnetic stripes, when

$$T(x = 4L_1, P_0) = 0. \tag{1}$$

The solution of Eq. (1) defines the critical power $P_0 = P_{th}$. One expects the monotonous increase of C with the increase of P_0; however, at the $P_0 = 23$ dBm the coefficient C as well as the coupling length L starts to decrease [see Fig. 4(c)]. This behavior can be attributed to the nonlinear magnon-magnon scattering processes, which are known to be highly efficient in YIG films and lead to the nonlinear damping of spin waves [25]. From the experimental data, which are depicted in Fig. 4(c) with triangles, it is seen that, at $P_{th} = 18$ dBm, the power is divided equally between S_1 and S_2. It is worth noting that the numerical simulation predicts the critical value of $P_{th} = 17$ dBm, which is in a good accordance with the experimental value.

The physical origin of the spin-wave coupling in SCMS is in the overlap of each stripe with the exponentially decaying tail of the spin-wave modes supported by the other stripe [16]. Furthermore, it was shown by Demidov [37] that in the Damon-Eshbach propagation geometry the nonlinearity acts in the opposite way to the linear diffraction decreasing the transverse spin-wave mode size. Figure 4(d) demonstrates the mode profile of each separated magnetic stripe at the input power 5 dBm (dotted curves) and 23 dBm (solid curves). The overlap of mode profiles is schematically depicted in Fig. 4(d) with the shaded area. Thus the MSSW field distribution transforms with the power increase, and the value of spin-wave wave vector is changed. Nonlinear eigenmode profiles were calculated using the iterative FEM simulation with the local mesh refinement [52] (the minimal element size of the mesh was 0.0188 μm, the maximum element growth rate was 1.25, and the curvature factor was 0.25) taking into account the local magnetization decrease with the profile corresponding to the linear eigenmode and nonuniform internal magnetic field profile, calculated via the micromagnetic simulation. The theory of the magnetodipolar interaction in the array of magnetic nanodots [70] can also be used to calculate SW coupling; however, in the case of Damon-Eschbach geometry it is impossible to apply this theoretical approach due to the nonuniform and asymmetric magnetic field profile in each magnetic stripe. We also take into account only the first SW mode of magnetic stripe due to the fact that for the higher order spin-wave mode the dynamic stray field produced by the spin-wave mode is decreased [15].

As seen from Fig. 4(d) the transverse width along y coordinate of the mode profiles of each separated stripe $\Phi_{1,2}(y, f, P_0)$ are decreased with the power increase. This leads to the decrease of the overlap integral between the modes in each SCMS:

$$C(f, P_0) = \frac{\int \Phi_1(y, f, P_0)\Phi_2(y, f, P_0)\,dy}{\sqrt{\int \Phi_1^2(y, f, P_0)\,dy \int \Phi_2^2(y, f, P_0)\,dy}}. \tag{2}$$

The integrals in (2) are taken along the line $-w - d/2 \leqslant y \leqslant w + d/2$. The calculated amplitude dependence of the overlap integral is shown in Fig. 4(e) with solid curve. The monotonic decrease of C with the increase of P_0 qualitatively elucidates the behavior of $L(P_0)$. It should be noted that we neglect the phase shift between the modes Φ_1 and Φ_2 in Eq. (2).

IV. PHENOMENOLOGICAL MODEL OF NONLINEAR SPIN-WAVE COUPLING

A. Particular form of coupled Ginzburg-Landau equations

The second mechanism contributing to the phenomena of spin-wave switching in SCMSs is the nonlinear phase shift of propagating SW [27–29,32,71]. To describe the propagation of nonlinear spin waves in the magnonic stripes and define the nonlinear spin-wave phase shift, we use the slowly varying envelope approximation approach usually employed in the physics of optical solitons and nonlinear waves [63]. It is known that there are two theoretical formalisms used to describe the nonlinear spin-wave coupling in the ferromagnetic films: the coupled Schrödinger equations (NSE) [25,72] and the particular form of the coupled Ginzburg-Landau equations (GLE) [36,63,71,73–77]. The latter is usually considered as a dissipative extension of the conservative NSE, which describes weakly nonlinear wave phenomena [74].

Next, we describe the spin-wave coupling in two adjacent magnetic stripes based on our assumption of the presence of nonlinear damping, which strongly influences the SW behavior. Thus we propose the phenomenological model based on a particular case of the GLE, which is also used in nonlinear optics [63,78]. The particular form of two coupled GLE [76] can be obtained from the Landau-Lifshitz equation for the magnetization dynamics taking into account Kerr-type nonlinearity [36,45,75,79], i.e., the decrease of the effective saturation magnetization: $M \approx M_0[1 - (m_x^2 + m_z^2)/(2M_0^2)] = M_0(1 - \varphi^2/2)$. Spin-wave power can be estimated asymptotically as [27,29,80] $P_{\text{in}} \approx |\varphi|^2 M_0^2 v_g w_{\text{eff}} t_1$, where v_g is the group velocity of MSSW in the magnetic stripe of effective width $w_{\text{eff}\,f}$; $\varphi = \varphi_0$ is the initial amplitude of MSSW for the numerical integration of coupled GLEs. Taking into account the radiation resistance for the lowest-order transverse mode of MSSW [26,81–84], excited by a shorted microstrip transmission line, we can estimate the value of P_{in} from experimental value P_0 via the SW and microstrip transducer coupling analysis [26].

The system of two coupled GLEs reads as

$$i\frac{d\Phi_{1,2}}{dx} = k\Phi_{1,2} + \kappa\Phi_{2,1} + (\zeta - i\nu_2)|\Phi_{1,2}|^2\Phi_{1,2} - i\nu_1\Phi_{1,2}, \tag{3}$$

where $\Phi_{1,2} = \Phi_{1,2}(x)|_{y=y_{1,2}}$ is the dimensionless SW amplitude along x axis, $y_{1,2}$ denotes the central position inside stripe S_1 and S_2, correspondingly, $k = k(f)$ is the wave number of SW propagating in the separate magnetic stripe, $\kappa = \kappa(f) = \beta C(f) \approx |k_s(f) - k_{as}(f)|$ is the coupling coefficient between the SW in the adjacent stripes, β is the proportionality coefficient, $\zeta = dk/d\varphi^2$ is the nonlinear coefficient, which was defined from the assumption of the magnetization reduction from the Damon-Eschbach dispersion of SW [27,48], $\nu_1 = \frac{1}{v_g}|\frac{\partial\omega}{\partial H_i}|\frac{\Delta H}{2}$ and $\nu_2 = \frac{1}{v_g^2}\zeta\frac{\Delta H}{2}|\frac{\partial\omega}{\partial H_i}||\frac{\partial^2\omega}{\partial k^2}|$ are the SW linear and nonlinear damping, correspondingly, and $\omega = 2\pi f$ is angular frequency. The ferromagnetic resonance linewidth is experimentally determined to be $\Delta H = 0.54$ Oe at the frequency of 9.7 GHz.

B. Nonlinear spin-wave phase shift

Next, by the direct numerical integration of Eq. (3) we compute the values of L and T as a function of input power. The dashed curves in Figs. 4(a) and 4(b) show the results of numerical simulation, which clearly exhibits a good agreement with the experimental values. The wave number k, coupling coefficient κ, and coefficient β were defined from FEM simulation. We note also that the micromagnetic simulations demonstrate a good agreement with BLS data [open circles in Figs. 4(a) and 4(b)], whereas the FEM simulation predicts only the monotonous growth of coupling length with the power increase. The important point is that the introduction of nonlinear damping leads to the increase of the power threshold P_{th} of spin-wave switching in the coupled GLEs rather than that for the coupled NSEs.

Moreover, the results of the nonlinear phase shift calculated by coupled GLEs demonstrate that the differential nonlinear phase shift in the stripe S_1 is $\Delta\phi_{\text{NL1}}(f_1) = \Delta\phi_{\text{th}} \approx 2.8\pi$ rad at the power value of P_{th}, which is in a good accordance for the optical one-beat length directional coupler [85]. It should be noted that the nonlinear phase shift in the first stripe is greater than that for the second stripe $\Delta\phi_{\text{NL1}} > \Delta\phi_{\text{NL2}}$ in the range of spin-wave power $0 < P_0 < 30$ dBm and $\Delta\phi_{\text{NL1}} - \Delta\phi_{\text{NL2}} \approx \pi$ at $P_0 = P_{\text{th}}$. The latter explains the intensity-dependent switching in the terms of the interference of the symmetrical and antisymmetrical eigenmodes. Moreover, we emphasize that the multimode pattern of spin-wave intensity [see Figs. 2(a) and 2(b)] in S_1 changes to almost single-mode regime as the power exceeds the P_{th} due to interference of width modes of separate stripe [37] [see Fig. 2(c)]. This effect also contributes to the growth of C with the power increase. We plot the experimentally measured data $\Delta\phi_{\text{NL1}}(P_0)$ with open circles in Fig. 4(d). The nonlinear phase shift was measured in the output section of the stripe S_1 using the microwave spectroscopy technique [23] based on VNA. The experiment and simulation consistently reveal the phase dependency of the SW power.

C. Power threshold power of spin-wave switching

Finally, we discuss the results of numerical simulation, which can verify the power-controlled switching regime and explain the experimental data [$L(P_0)$ and $C(P_0)$]. We estimate the decrease of the effective saturation magnetization δM_s [blue dashed line in Fig. 5(a)] with the increase of amplitude of magnetization [25,27] h_0: $\delta M_s = M_0 - M_s \approx M_0\gamma^2 h_0^2/(2\alpha^2\omega^2)$, where $\alpha = \frac{1}{\omega}|\frac{\partial\omega}{\partial H_i}|\frac{\Delta H}{2} = 1.15 \times 10^{-5}$ is the Gilbert damping parameter [25,86]. Therefore, we compute the coupling length as a function of saturation magnetization M_s. The data in Fig. 5(a) (open circles and fitting with the red curve) demonstrate the decrease of L as M_s increases and reaches the M_0. Thus the $L(h_0)$ can be estimated from the iterative FEM simulation.

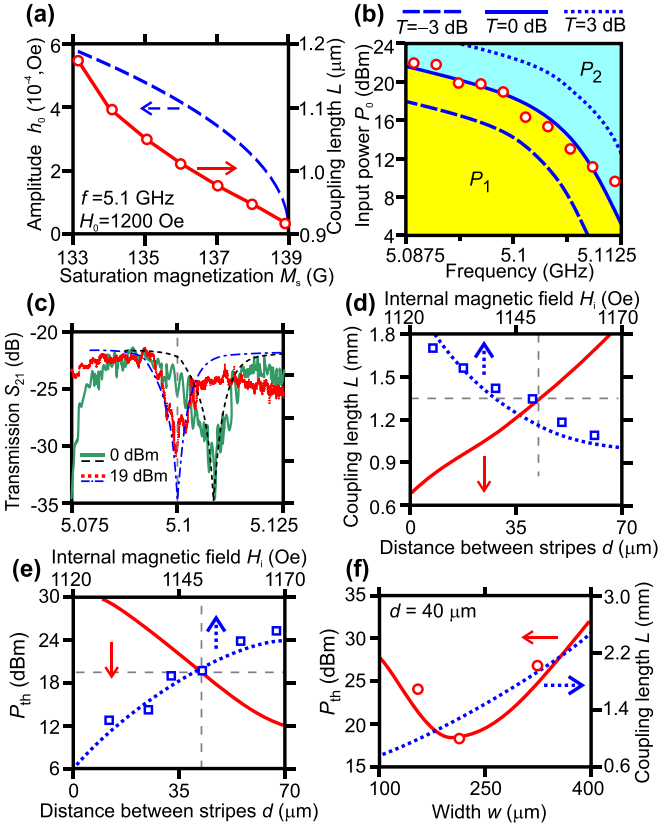

FIG. 5. (a) Dynamic amplitude of SW h_0 (solid curve) and coupling length (dashed curve) as a function of saturation magnetization in YIG. (b) The map of $P_0(f)$ demonstrating the regimes of spin-wave dynamics. Yellow region corresponds to the SW transmission through the first magnetic stripe, blue—to the second. The dashed, solid, and dotted curves correspond to the values of T, denoted at the top of map. (c) Transmission of SW through the first stripe S_1 measured with VNA in linear (solid green curve) and nonlinear (dotted red curve) regime. Calculation results are shown with dashed and dash-dotted curves. (d) Coupling length as a function of distance between stripes (solid curve) and internal magnetic field in the center of the stripe (dotted curve—simulation; open squares—BLS experiment). (e) Threshold power P_{th} of spin-wave switching as a function of spacing between stripes and internal magnetic field. (f) Threshold power (solid curve) and coupling length (dotted curve) as a function of the stripes' width. Open circles denote the experimental data.

We plot the color-coded regime map in Fig. 5(b) demonstrating the signal switching from the S_1 to the S_2 frequency dependence of the nonlinear switching threshold $P_{th}(f)$. Here the blue solid, dashed, and dotted curves correspond to the conditions $T(P_0, f) = 0$ dBm, $T(P_0, f) = -3$ dBm, and $T(P_0, f) = 3$ dBm, respectively. As it is seen from Fig. 5(b) the value of P_{th} is decreased with the frequency increase; however, the monotonic growth of the coupling length L impedes the further lowering of the switching threshold.

Figure 5(c) shows the frequency dependence of the modulus of the transmission coefficient in the linear (green solid curve) and nonlinear (red dashed curve) regime, which was measured using the microwave spectroscopy, when the output transducer is placed at the end of the stripe S_1. The response shown for the SCMSs is typical of a whole class of devices involving the linear and nonlinear coupling between two copropagating modes [16,23,85]. The well-pronounced stop-band dip corresponds to the frequencies, at which the power of spin wave does not effectively return to the output section of the stripe S_1. The position of the dip is shifted in the low-frequency region with the spin-wave power increase. The calculated transmission for the linear and nonlinear regime are plotted with dashed and dashed-dotted curves, correspondingly, and are in good accordance with the experimental data.

Moreover, we emphasize that we consider only the linear contribution to the perturbing of magnetization in adjacent stripes, which arises from the overlap of the modal field with a parallel stripe. We neglect the nonlinear contribution in coupling, which arises due to the nonlinear interaction between the spin-wave modes in adjacent stripes [87]. The nonlinear coupling starts to work at the significant high power of propagated wave, and thus the nonlinear damping influences the spin-wave dynamics and cannot lead to the "nonlinear coupling" mechanism, i.e., as the power of spin wave increases the spin-wave damping also increases and this leads to the limitation of the functionality of the nonlinear coupler.

V. INFLUENCE OF GEOMETRY OF ADJACENT STRIPES ON NONLINEAR SPIN-WAVE COUPLING

It was shown in Sec. II B that the coupling length $L(f)$ defines the geometry of the all-magnonic spin-wave coupler. In the linear regime of SW propagation in the coupling section of the length b [see Fig. 1(a)], $L(f)$ should satisfy the condition $L(f) \leqslant b$. In the nonlinear regime the necessary criterion of intensity-dependent SW switching in SCMSs reads as

$$L_{NL}(f) \leqslant L(f) \leqslant L_d(f), \tag{4}$$

where L_{NL} is the characteristic length scale [88] provided the phase shift $\Delta\phi_{NL}(f)$ in nonlinear regime of SW propagation; $L_d = 1/\nu_1$ is the propagation length [25] of SW.

Therefore, we discuss here the design of the all-magnonic coupler and define the conditions of lowering of the power threshold for efficient spin-wave switching in the laterally parallel magnetic stripes.

Spacing between magnetic stripe defines the coupling length [16] and as a consequence has a significant effect on the switching power. Thus the increase of the distance between stripes d leads to the increase of L, as one can see from Fig. 5(e) (d is ranging between 0 and 70 μm). When $d \to 0$ μm the coupling length $L \to L_{12}$, where $L_{12} = \pi/(k_1 - k_2)$; k_1 and k_2 are the wave numbers of the first and second transverse modes of MSSW in the stripe of the width [16] of $2w$. We also demonstrate the tuning of the coupling length by the factor of 1.8 with the variation of the magnetic field from 1120 Oe to 1170 Oe [see Fig. 5(e)]. The blue dotted line in Fig. 5(e) shows the results of FEM simulation and open squares depict the data, which are extracted from BLS measurements.

The decrease of the stripes' width w leads to the decrease of the group velocity v_g of the MSSW [see Fig. 1(c) for both symmetric and antisymmetric modes] and as a result leads to the increase of the nonlinear phase shift $\Delta\phi_{NL1}$, which can be estimated with Eq. (7) from Ref. [89]. This leads to the decrease of the P_{th} with the decrease of w. From the other hand, as shown in Fig. 1(c), the decrease of w leads to the

increase of $\Delta k = |k_s(f, P_0) - k_{as}(f, P_0)|$ and as a consequence to the increase of P_{th}. It should be also taken into account that the relative effective gap between the stripes d_{eff}/d is increased with the decrease of w [see the inset in Fig. 1(a)]. As a result, the value of overlap integral C is decreased. This leads also to the decrease of the threshold power P_{th} with the decrease of w.

Figure 5(f) demonstrates the well-defined minima of the dependency $P_{th}(d)$ due to the effect of the above-mentioned mechanisms. Thus the optimal values of the SCMS's width are in the range $125 < w < 275$ μm for the YIG thickness of 7.7 μm. Thus it should be noted that in Ref. [22] the absence of the nonlinear spin-wave switching can be explained with the relatively high waveguide width of 720 μm, which was insufficient to reach the appropriate value of $\Delta\phi_{NL}$ even at the input power of $P_0 = 26$ dBm.

We have to note that the variation of the angle of magnetization leads to the variation of the value of overlap integral and thus to the variation of coupling length. However, in the geometry of the backward volume magnetostatic wave (BVMSW) the value of the coupling length is higher than for MSSW; thus the threshold power is also higher. Therefore, the power requirement to the all-magnonic switching could be reduced by using the MSSW and the appropriate geometry design.

VI. CONCLUSIONS

In conclusion, we experimentally observe the intensity-dependent switching in side-coupled YIG stripes. Using the Brillouin light scattering technique and microwave spectroscopy, we demonstrate the nonlinear spin-wave coupling. We find that the increase of the input microwave signal level leads to the variation of the power transmission coefficient between magnonic stripes. The developed analytical model, taking into account the spin-wave modes transformation and nonlinear spin-wave phase shift, elucidates the mechanisms of nonlinear spin-wave coupling between the adjacent magnonic stripes and predicts the optimal geometry design of the directional magnonic coupler. This make the studied phenomenon very promising for applications of side-coupled magnetic stripes in all-magnonic signal processing based on spin-wave-based integrated circuits and magnonic networks. Additionally, these results show the possibility of expansion of the emerging field of magnonics and provide opportunities for nonlinear magnonics, where the nonlinear effects play the crucial role for the spin-wave transport in the patterned magnetic structures.

ACKNOWLEDGMENTS

Structure fabrication, microwave measurements, and numerical simulation were supported by a grant from the Russian Science Foundation (No. 16-19-10283). The numerical simulation was supported partially by the Russian Foundation for Basic Research (No. 16-37-00217). A.V.S. and S.E.S. acknowledge support from the Scholarship of the President of RF (No. SP-313.2015.5) and Grant of the President of RF (No. MK-5837.2016.9). A.V.S. is thankful for fruitful discussions with N. M. Ryskin, A. B. Ustinov, M. A. Morozova (coupled wave theory and Ginzburg-Landau equations), V. E. Demidov (nonlinear transformation of spin-wave profile), M. Kostylev, A. N. Slavin (nonlinear stray field profiles), and Yu. A. Filimonov (nonlinear processes in YIG and four-magnon decay).

[1] V. V. Kruglyak, S. O. Demokritov, and D. Grundler, J. Phys. D: Appl. Phys. **43**, 264001 (2010).
[2] V. E. Demidov, S. Urazhdin, A. Zholud, A. V. Sadovnikov, A. N. Slavin, and S. O. Demokritov, Sci. Rep. **5**, 8578 (2015).
[3] S. A. Nikitov, D. V. Kalyabin, I. V. Lisenkov, A. N. Slavin, Y. N. Barabanenkov, S. A. Osokin, A. V. Sadovnikov, E. N. Beginin, M. A. Morozova, Y. P. Sharaevsky, Y. A. Filimonov, Y. V. Khivintsev, S. L. Vysotsky, V. K. Sakharov, and E. S. Pavlov, Phys. Usp. **185**, 1099 (2015).
[4] A. V. Chumak, V. I. Vasyuchka, A. A. Serga, and B. Hillebrands, Nat. Phys. **11**, 453 (2015).
[5] H. Yu, O. D. A. Kelly, V. Cros, R. Bernard, P. Bortolotti, A. Anane, F. Brandl, F. Heimbach, and D. Grundler, Nat. Commun. **7**, 11255 (2016).
[6] S. Klingler, P. Pirro, T. Bracher, B. Leven, B. Hillebrands, and A. V. Chumak, Appl. Phys. Lett. **105**, 152410 (2014).
[7] A. Khitun, M. Bao, and K. L. Wang, J. Phys. D: Appl. Phys. **43**, 264005 (2010).
[8] ITRS, International Technology Roadmap for Semiconductors (ITRS), 2015 ed., http://www.itrs2.net/itrs-reports.html (accessed 1 April 2017).
[9] M. Evelt, V. E. Demidov, V. Bessonov, S. O. Demokritov, J. L. Prieto, M. Muñoz, J. B. Youssef, V. V. Naletov, G. de Loubens, O. Klein, M. Collet, K. Garcia-Hernandez, P. Bortolotti, V. Cros, and A. Anane, Appl. Phys. Lett. **108**, 172406 (2016).
[10] V. E. Demidov, S. Urazhdin, A. Zholud, A. V. Sadovnikov, and S. O. Demokritov, Appl. Phys. Lett. **106**, 022403 (2015).
[11] A. V. Sadovnikov, S. Davies, S. Grishin, V. Kruglyak, D. Romanenko, Y. Sharaevskii, and S. Nikitov, Appl. Phys. Lett. **106**, 192406 (2015).
[12] A. K. Ganguly and C. Vittoria, J. Appl. Phys. **45**, 4665 (1974).
[13] H. Sasaki and N. Mikoshiba, Electron. Lett. **15**, 172 (1979).
[14] H. Sasaki and N. Mikoshiba, J. Appl. Phys. **52**, 3546 (1981).
[15] G. Gubbiotti, S. Tacchi, G. Carlotti, P. Vavassori, N. Singh, S. Goolaup, A. O. Adeyeye, A. Stashkevich, and M. Kostylev, Phys. Rev. B **72**, 224413 (2005).
[16] A. V. Sadovnikov, E. N. Beginin, S. E. Sheshukova, D. V. Romanenko, Y. P. Sharaevskii, and S. A. Nikitov, Appl. Phys. Lett. **107**, 202405 (2015).
[17] C. S. Davies, A. Francis, A. V. Sadovnikov, S. V. Chertopalov, M. T. Bryan, S. V. Grishin, D. A. Allwood, Y. P. Sharaevskii, S. A. Nikitov, and V. V. Kruglyak, Phys. Rev. B **92**, 020408 (2015).
[18] A. V. Sadovnikov, E. N. Beginin, S. A. Odincov, S. E. Sheshukova, Y. P. Sharaevskii, A. I. Stognij, and S. A. Nikitov, Appl. Phys. Lett. **108**, 172411 (2016).

[19] A. Y. Annenkov and S. V. Gerus, J. Commun. Technol. Electron. **41**, 196 (1996).

[20] A. Y. Annenkov, S. V. Gerus, and S. I. Kovalev, Tech. Phys. **43**, 216 (1998).

[21] M. A. Morozova, S. V. Grishin, A. V. Sadovnikov, Y. P. Sharaevskii, and S. A. Nikitov, IEEE Trans. Magn. **50**, 1 (2014).

[22] A. V. Sadovnikov, E. N. Beginin, M. A. Morozova, Y. P. Sharaevskii, S. V. Grishin, S. E. Sheshukova, and S. A. Nikitov, Appl. Phys. Lett. **109**, 042407 (2016).

[23] A. V. Sadovnikov, A. A. Grachev, E. N. Beginin, S. E. Sheshukova, Y. P. Sharaevskii, and S. A. Nikitov, Phys. Rev. Appl. **7**, 014013 (2017).

[24] N. Rosanov, Phys. Usp. **43**, 421 (2000).

[25] A. G. Gurevich and G. A. Melkov, *Magnetization Oscillations and Waves* (CRC-Press, London, New York, 1996).

[26] D. D. Stancil and A. Prabhakar, *Spin Waves: Theory and Applications* (Springer, New York, 2009).

[27] A. K. Zvezdin and A. F. Popkov, Zh. Eksp. Teor. Fiz. **84**, 606 (1983).

[28] P. E. Zilberman, S. A. Nikitov, and A. G. Temiryazev, JETP Lett. **42**, 110 (1985).

[29] A. D. Boardman, S. A. Nikitov, and N. A. Waby, Phys. Rev. B **48**, 13602 (1993).

[30] M. Chen, M. A. Tsankov, J. M. Nash, and C. E. Patton, Phys. Rev. Lett. **70**, 1707 (1993).

[31] M. Bauer, O. Büttner, S. O. Demokritov, B. Hillebrands, V. Grimalsky, Yu. Rapoport, and A. N. Slavin, Phys. Rev. Lett. **81**, 3769 (1998).

[32] C. E. Patton, P. Kabos, H. Xia, P. A. Kolodin, R. Staudinger, B. A. Kalinikos, and N. G. Kovshikov, J. Magn. Soc. Jpn. **23**, 605 (1999).

[33] A. N. Slavin, O. Buttner, M. Bauer, S. O. Demokritov, B. Hillebrands, M. M. Kostylev, B. A. Kalinikos, V. V. Grimalsky, and Y. Rapoport, Chaos **13**, 693 (2003).

[34] S. O. Demokritov *et al.*, Nature (London) **426**, 159 (2003).

[35] M. Wu, M. A. Kraemer, M. M. Scott, C. E. Patton, and B. A. Kalinikos, Phys. Rev. B **70**, 054402 (2004).

[36] M. M. Scott, M. P. Kostylev, B. A. Kalinikos, and C. E. Patton, Phys. Rev. B **71**, 174440 (2005).

[37] V. E. Demidov, P. Rekers, B. Mahrov, and S. O. Demokritov, Appl. Phys. Lett. **89**, 212501 (2006).

[38] V. E. Demidov, U.-F. Hansen, O. Dzyapko, N. Koulev, S. O. Demokritov, and A. N. Slavin, Phys. Rev. B **74**, 092407 (2006).

[39] V. E. Demidov, U.-H. Hansen, and S. O. Demokritov, Phys. Rev. Lett. **98**, 157203 (2007).

[40] V. E. Demidov, J. Jersch, K. Rott, P. Krzysteczko, G. Reiss, and S. O. Demokritov, Phys. Rev. Lett. **102**, 177207 (2009).

[41] V. E. Demidov, H. Ulrichs, S. O. Demokritov, and S. Urazhdin, Phys. Rev. B **83**, 020404 (2011).

[42] H. Suhl, J. Phys. Chem. Solids **1**, 209 (1957).

[43] V. E. Demidov, M. Evelt, V. Bessonov, S. O. Demokritov, J. L. Prieto, M. Muñoz, J. Ben Youssef, V. V. Naletov, G. de Loubens, O. Klein, M. Collet, P. Bortolotti, V. Cros, and A. Anane, Sci. Rep. **6**, 32781 (2016).

[44] J. D. Adam, L. E. Davis, G. F. Dionne, E. F. Schloemann, and S. N. Stitzer, IEEE Trans. Microwave Theory Tech. **50**, 721 (2002).

[45] M. M. Scott, C. E. Patton, M. P. Kostylev, and B. A. Kalinikos, J. Appl. Phys. **95**, 6294 (2004).

[46] U.-H. Hansen, V. E. Demidov, and S. O. Demokritov, Appl. Phys. Lett. **94**, 252502 (2009).

[47] S. Sheshukova, E. Beginin, A. Sadovnikov, Y. Sharaevsky, and S. Nikitov, IEEE Magn. Lett. **5**, 1 (2014).

[48] R. W. Damon and J. Eschbach, J. Phys. Chem. Solids **19**, 308 (1961).

[49] S. N. Bajpai, J. Appl. Phys. **58**, 910 (1985).

[50] A. Weierholt, A. Mickelson, and S. Neegard, IEEE J. Quantum Electron. **23**, 1689 (1987).

[51] M. Koshiba, K. Hayata, and M. Suzuki, J. Lightwave Technol. **4**, 121 (1986).

[52] A. Sadovnikov and A. G. Rozhnev, Appl. Nonlin. Dyn. [Izvest. VUZ (in Russian)] **20**, 143 (2012).

[53] C. Kittel, J. Phys. Rad. **12**, 291 (1951).

[54] S. O. Demokritov, B. Hillebrands, and A. N. Slavin, Phys. Rep. **348**, 441 (2001).

[55] S. O. Demokritov and V. E. Demidov, IEEE Trans. Magn. **44**, 6 (2008).

[56] V. E. Demidov and S. O. Demokritov, IEEE Trans. Magn. **51**, 1 (2015).

[57] V. E. Demidov, S. O. Demokritov, K. Rott, P. Krzysteczko, and G. Reiss, Phys. Rev. B **77**, 064406 (2008).

[58] P. Clausen, K. Vogt, H. Schultheiss, S. Schäfer, B. Obry, G. Wolf, P. Pirro, B. Leven, and B. Hillebrands, Appl. Phys. Lett. **99**, 162505 (2011).

[59] A. A. Maier, Sov. J. Quantum Electron. **12**, 1490 (1982).

[60] S. Jensen, IEEE J. Quantum Electron. **18**, 1580 (1982).

[61] S. Wabnitz, E. M. Wright, C. T. Seaton, and G. I. Stegeman, Appl. Phys. Lett. **49**, 838 (1986).

[62] A. A. Maier, Phys. Usp. **39**, 1109 (1996).

[63] G. Agrawal, *Applications of Nonlinear Fiber Optics* (Elsevier Science, Amsterdam, 2010).

[64] D. A. Smirnova, A. Gorbach, I. V. Iorsh, I. Shadrivov, and Y. Kivshar, Phys. Rev. B **88**, 045443 (2013).

[65] M. J. Donahue and D. G. Porter, *OOMMF Users Guide, 1.0* (NISITR, Gaithersburg, MD, 1999), Vol. 6376, p. 320.

[66] L. Landau and E. Lifshitz, Phys. Z. Sowjetunion **8**, 153 (1935).

[67] O. Karlqvist, Trans. R. Inst. Technol. Stockholm **86**, 3 (1954).

[68] C. S. Davies, A. V. Sadovnikov, S. V. Grishin, Y. P. Sharaevsky, S. A. Nikitov, and V. V. Kruglyak, IEEE Trans. Magn. **51**, 1 (2015).

[69] S. L. Hahn, *Hilbert Transforms in Signal Processing* (Artech House, Boston, 1996).

[70] R. Verba, G. Melkov, V. Tiberkevich, and A. Slavin, Phys. Rev. B **85**, 014427 (2012).

[71] A. B. Ustinov and B. A. Kalinikos, Appl. Phys. Lett. **93**, 102504 (2008).

[72] S. E. Sheshukova, M. A. Morozova, E. N. Beginin, Y. P. Sharaevskii, and S. A. Nikitov, Phys. Wave Phenom. **21**, 304 (2013).

[73] V. Ginzburg and L. D. Landau, Zh. Eksp. Teor. Fiz. **20**, 1064 (1950).

[74] A. C. Newell and J. V. Moloney, *Nonlinear Optics* (Addison-Wesley, Redwood City, CA, 1992).

[75] V. S. Lvov, *Wave Turbulence Under Parametric Excitation* (Springer, Berlin, 1994).

[76] I. S. Aranson and L. Kramer, Rev. Mod. Phys. **74**, 99 (2002).

[77] B. Malomed, O. Dzyapko, V. Demidov, and S. Demokritov, Phys. Rev. B **81**, 024418 (2010).

[78] Y. S. Kivshar and G. Agrawal, *Optical Solitons: From Fibers to Photonic Crystals* (Academic Press, New York, 2003).
[79] A. B. Ustinov, V. S. Tiberkevich, G. Srinivasan, A. N. Slavin, A. A. Semenov, S. F. Karmanenko, B. A. Kalinikos, J. V. Mantese, and R. Ramer, J. Appl. Phys. **100**, 093905 (2006).
[80] B. A. Kalinikos, N. G. Kovshikov, and A. N. Slavin, Zh. Eksp. Teor. Fiz. **94**, 159 (1988).
[81] A. K. Ganguly and D. C. Webb, *Microwave Symposium, 1975 IEEE-MTT-S International* (IEEE, New York, 1975), pp. 368–370.
[82] P. R. Emtage, J. Appl. Phys. **49**, 4475 (1978).
[83] V. F. Dmitriev and B. A. Kalinikos, Izvest. VUZ Fiz. (in Russian) **31**, 24 (1988).
[84] P. Kaboš and V. Stalmachov, *Magnetostatic Waves and Their Application* (Chapman & Hall, London, 1994).
[85] G. I. Stegeman and R. H. Stolen, J. Opt. Soc. Am. B **6**, 652 (1989).
[86] T. Gilbert, Phys. Rev. **100**, 1243 (1955).
[87] Y. Chen, A. W. Snyder, and D. N. Payne, IEEE J. Quantum Electron. **28**, 239 (1992).
[88] G. Srinivasan and A. N. Slavin, *High Frequency Processes in Magnetic Materials* (World Scientific, Singapore, 1995).
[89] A. B. Ustinov and B. A. Kalinikos, Appl. Phys. Lett. **89**, 172511 (2006).